Electronic Supplementary Material (ESI) for Physical Chemistry Chemical Physics.

# Supporting Information:

# Excitation wavelength-dependent EPR study on the influence of the conformation of multiporphyrin arrays on triplet state delocalization

Claudia E. Tait,[a,†]* Patrik Neuhaus,[b] Martin D. Peeks,[b] Harry L. Anderson,[b] Christiane R. Timmel[a]*

[a]Department of Chemistry, Centre for Advanced Electron Spin Resonance, University of Oxford, South Parks Road, Oxford OX1 3QR, UK.

[b]Department of Chemistry, Chemistry Research Laboratory, University of Oxford, 12 Mansfield Road, Oxford OX1 3TA, UK.

[†] Present address: Department of Chemistry, University of Washington, Seattle, WA 98195, USA

## Experimental Methods

### Synthesis and sample preparation

The zinc porphyrin oligomers (**P1** to **P4**) depicted in Figure S1 were synthesized according to a previously published procedure.[1, 2] The structure and purity of the synthesized compounds were confirmed by NMR, mass spectrometry (MALDI-ToF), UV-vis and analytical GPC. The EPR measurements were performed on 50-200 μM solutions in MeTHF: pyridine 10:1 or in *o*-terphenyl. The solutions were degassed by several freeze-pump-thaw cycles and shock-frozen in liquid $N_2$.

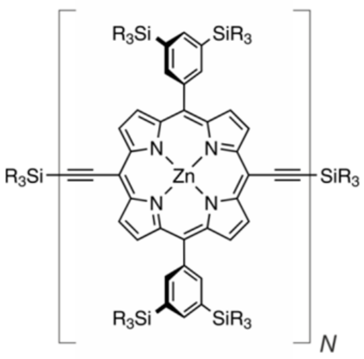

**Figure S1.** Molecular structure of the porphyrin oligomers investigated in this study (*N*=1-4, R=*n*-hexyl ($C_6H_{13}$)).

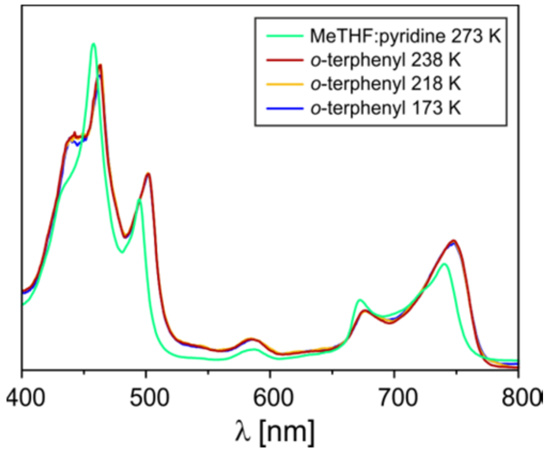

**Figure S2.** UV-vis spectra of **P2** recorded in MeTHF:pyridine 10:1 at 273 K and in *o*-terphenyl at 238, 218 and 173 K.

### Time-resolved EPR

The time-resolved EPR experiments were performed at X-band on a Bruker Elexsys 680 spectrometer equipped with a helium gas-flow cryostat from Oxford instruments. Laser excitation at 532 nm was provided by the second harmonic of an Nd:YAG laser (Surelite Continuum) with a repetition rate of 10 Hz. Light depolarized with an achromatic depolarizer was used unless otherwise stated. TR-EPR experiments were performed by direct detection with the transient recorder without lock-in amplification; the microwave power was 0.2 mW. The laser background signal was removed by 2D baseline-correction determined based on the off-resonance transients. The spectra were integrated over the first 2 μs after the laser flash. Experiments were typically performed at 20 K, but no changes in the spectral shape were observed at temperatures between about 100 and 5 K.

Experiments with different excitation wavelengths were performed with an Opotek Opolette Opto-parametric Oscillator (OPO) tuneable laser (20 Hz repetition rate) at wavelengths corresponding to the region of the Q-bands in the UV-vis spectra.

**Table S1.** ZFS parameters and relative sublevel populations for **P1-P4** determined from simulation of the experimental transient EPR spectra recorded at a wavelength corresponding to the planar conformation.[2]

| | \|*D*\| [MHz] | \|*E*\| [MHz] | $p_X : p_Y : p_Z$ |
|---|---|---|---|
| **P1** | 898±5 | 161±2 | 0.05 : 0.00 : 0.95 |
| **P2** | 1117±9 | 284±2 | 0.88 : 0.00 : 0.12 |
| **P3** | 1169±7 | 269±2 | 0.46 : 0.00 : 0.54 |
| **P4** | 1195±8 | 273±2 | 0.28 : 0.00 : 0.72 |

### ENDOR

X-band pulse ENDOR measurements were performed on a Bruker Elexsys 680 spectrometer with a Bruker EN 4118X-MD4 resonator. The measurements were performed at 20 K and with laser excitation as previously described. The repetition rate of the pulse experiments was determined by the laser repetition rate of 10 Hz (20 Hz for measurements with the OPO).

The $^1$H Mims ENDOR spectra were recorded with the pulse sequence $\frac{\pi}{2} - \tau - \frac{\pi}{2} - T - \frac{\pi}{2} - \tau -$ echo with mw pulse lengths of $t_{\pi/2}$=24 ns, τ =120, 160, 200 ns and a radiofrequency pulse length of 15 μs; the RF power was adjusted based on a nutation experiment. The ENDOR spectra were recorded at the canonical field positions of the triplet state EPR spectrum;

spectra were recorded for three different τ values (120, 160 and 200 ns) and summed to prevent distortions by blind spots.

### Computational methods

DFT geometry optimizations of the triplet excited state structures for **P1** and **P2** were performed in ORCA[3, 4] with the BP86 functional and the SV(P) basis set using the RI approximation with the auxiliary SV/C basis set. The $Si(C_6H_{13})_3$ groups were replaced by hydrogen atoms and the resulting structures were optimized without symmetry constraints. For **P2**, a potential energy surface scan was performed by changing the dihedral angle between the two porphyrin units in 10° increments and optimizing the internal coordinates keeping the dihedral angle fixed. Single-point calculations with the EPRII basis set were performed for each conformation to determine the zero-field splitting and hyperfine parameters.

The zero-field splitting interaction parameters were calculated according to a procedure published by Sinnecker et al.,[5] using the B3LYP functional and the EPRII basis set[6] and calculating the spin-spin contribution to the ZFS using UNO determinants. The hyperfine parameters were calculated with the B3LYP functional and the EPRII basis set, purposely developed for the calculation of EPR hyperfine interaction values, for the C, N and H nuclei[6-8] and the 6-31G(d) basis set for Zn.

### Simulation of the excitation-wavelength dependence of P2

The spin-polarized powder triplet state spectra were simulated using EasySpin's *pepper* routine.[9] The zero-field splitting parameters *D* and *E* as well as the relative population probabilities at zero-field for the planar conformations of **P1** and **P2** were determined by least-square fitting of the experimental transient EPR data. The energy ordering of the triplet sublevels was chosen as |Z|>|X|>|Y|.

In order to interpret the changes in the time-resolved EPR spectra as well as the ENDOR spectra, model calculations were performed to reproduce and explain the observed changes. The procedure used for these calculations is outlined in Figure S4.

The simulation of the contribution of different conformations of the porphyrin dimer at different wavelengths requires the knowledge of the "pure" EPR and ENDOR spectra corresponding to each conformation. Due to the extensive overlap of their absorption bands, the experimental determination of these spectra was not possible. They were instead estimated based on DFT calculations and the experimental results obtained for the planar conformation of **P2** at the high wavelength edge, and for **P1**, the latter as a model of the twisted conformation with localization of the triplet state on a single unit.

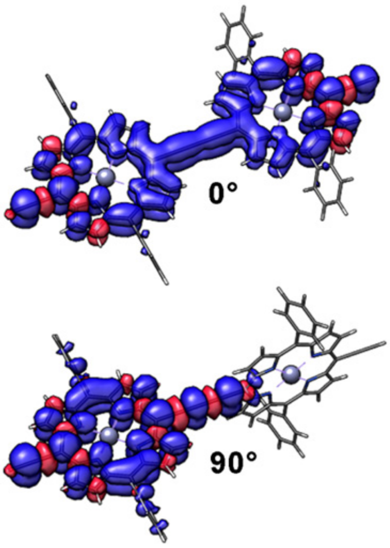

**Figure S3.** Mulliken spin densities for the planar (0°) and twisted (90°) conformations of **P2** calculated at the B3LYP/EPRII level of theory.

**Table S2.** DFT spin densities on the two porphyrin units and DFT-derived zero-field splitting parameters (B3LYP/EPRII).

| | DFT spin densities | *D* [MHz] | *E* [MHz] |
|---|---|---|---|
| 0° | 0.50:0.50 | -606.93 | 73.20 |
| 10° | 0.32:0.67 | -581.84 | 94.03 |
| 20° | 0.28:0.72 | -563.61 | 102.27 |
| 30° | 0.23:0.77 | -537.02 | 117.01 |
| 40° | 0.19:0.81 | -519.78 | 127.27 |
| 50° | 0.13:0.87 | -485.54 | -150.92 |
| 60° | 0.10:0.90 | 477.33 | -153.56 |
| 70° | 0.08:0.92 | 482.31 | -144.41 |
| 80° | 0.06:0.94 | 484.64 | -139.14 |
| 90° | 0.06:0.94 | 485.15 | -137.41 |
| **P1**[10] | - | 492 | -120 |

**Table S3.** Zero-field splitting and relative sublevel population parameters used for the simulations shown in Figure S6 for structures with different dihedral angles between the two porphyrin units.

| | *D* [MHz] | *E* [MHz] | $p_X$:$p_Y$:$p_Z$ |
|---|---|---|---|
| 0° | -1120 | 280 | 1.00:0.00:0.00 |
| 10° | -1074 | 260 | 0.95:0.05:0.00 |
| 20° | -1040 | 244 | 0.91:0.09:0.00 |
| 30° | -991 | 225 | 0.90:0.10:0.00 |
| 40° | -959 | 210 | 0.89:0.11:0.00 |
| 50° | -896 | 189 | 0.90:0.10:0.00 |
| 60° | 881 | -179 | 0.00:0.08:0.92 |
| 70° | 890 | -174 | 0.00:0.07:0.93 |
| 80° | 894 | -168 | 0.00:0.06:0.94 |
| 90° | 895 | -161 | 0.00:0.06:0.94 |

The DFT calculations predict equal spin densities on the two porphyrin units for a dihedral angle of 0° and a gradual shift of the spin density onto one of the porphyrin units as the dihedral angle increases (Table S2 and Figure S3). The DFT-derived *D*-values (Table S2) decrease gradually for increasing dihedral angles, but the sign of the *D*-value and the orientation of the zero-field splitting tensor are predicted to change suddenly in the interval of dihedral angles from 50° to 60° (spin density distributions over the two porphyrin units of 0.87:0.13 and 0.90:0.10, respectively). The *D*- and *E*-values predicted for the conformation with the two porphyrin units at right angles to each other correspond approximately to the values calculated by DFT for the porphyrin monomer.

In order to calculate the time-resolved EPR spectra corresponding to the different conformations, the DFT-derived zero-field splitting parameter *D* was scaled based on the experimentally determined values for the planar conformation (the maximum |*D*|). This was based on the assumption that DFT predicts the relative changes in ZFS as a function of inter-porphyrin angle correctly, while it severely underestimates the magnitudes. The *E*-values were calculated from the *D*-values using the *E/D* ratios obtained by linear interpolation of the experimental E/D ratios of the porphyrin monomer (*E/D*=0.18) and dimer (*E/D*=0.25). The values used for the simulations are summarized in Table S3.

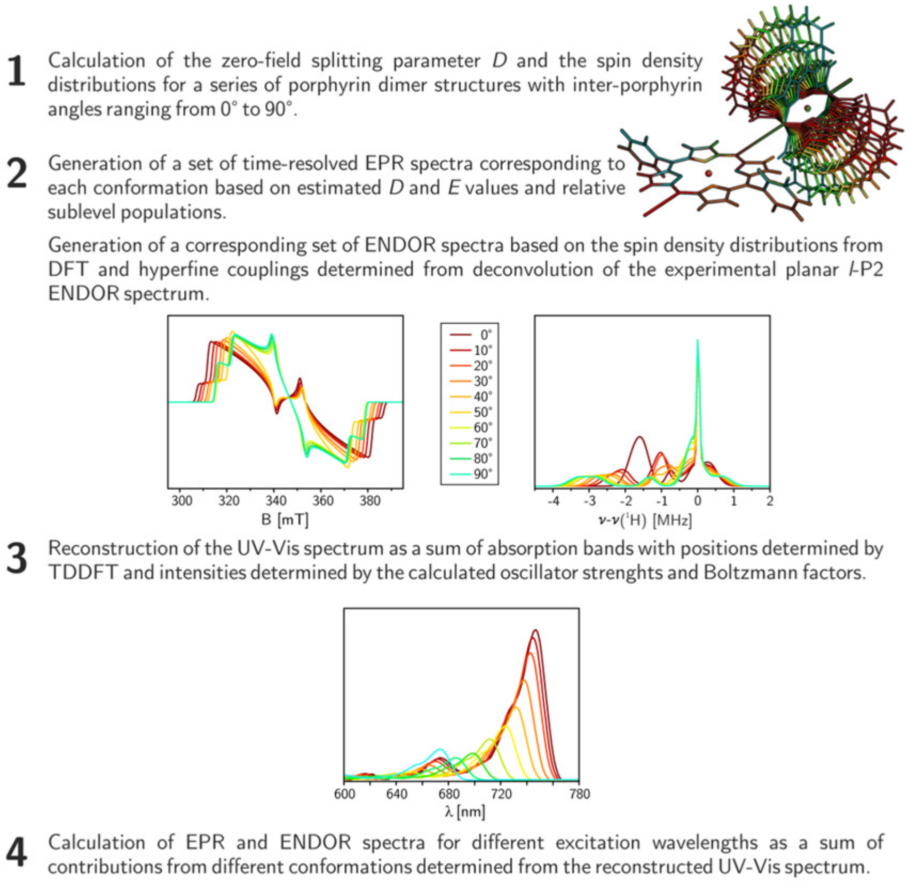

1 Calculation of the zero-field splitting parameter *D* and the spin density distributions for a series of porphyrin dimer structures with inter-porphyrin angles ranging from 0° to 90°.

2 Generation of a set of time-resolved EPR spectra corresponding to each conformation based on estimated *D* and *E* values and relative sublevel populations.

Generation of a corresponding set of ENDOR spectra based on the spin density distributions from DFT and hyperfine couplings determined from deconvolution of the experimental planar *l*-P2 ENDOR spectrum.

3 Reconstruction of the UV-Vis spectrum as a sum of absorption bands with positions determined by TDDFT and intensities determined by the calculated oscillator strenghts and Boltzmann factors.

4 Calculation of EPR and ENDOR spectra for different excitation wavelengths as a sum of contributions from different conformations determined from the reconstructed UV-Vis spectrum.

**Figure S4.** Outline of the procedure used for the simulation of wavelength-dependent EPR and ENDOR spectra for **P2.**

The relative sublevel populations were predicted by assuming population to occur exclusively for the out-of-plane orientation of each porphyrin unit, as the direct zinc spin-orbit coupling contribution dominates ISC,[2] and by projecting the corresponding axes onto the zero-field splitting tensor axis system. The projections were weighted by the relative amount of spin density on each porphyrin unit.

The ENDOR spectra were recorded at a magnetic field of 379 mT, corresponding to the Z canonical transition for **P1** and to the X canonical position for **P2**. Due to the reorientation of the ZFS tensor between **P1** and **P2**, with an axis of maximum dipolar coupling Z shifting from the out-of-plane direction in **P1** to the long axis of the molecule in **P2**,[10] both the Z axis in **P1** and the X axis in **P2** correspond to the same direction in the molecular frame, i.e. the out-of-plane direction. In order to predict the ENDOR spectra for the different conformations, the change of the out-of-plane proton hyperfine couplings as a function of dihedral angle has to be determined. The hyperfine couplings for the out-of-plane orientation for the porphyrin dimer were determined by deconvolution of the ENDOR spectrum with a series of Gaussians. The ENDOR spectra corresponding to the different conformations were then reconstructed by scaling the hyperfine couplings, determining the position of the Gaussians, based on the ratio of spin densities on the two porphyrin units predicted by DFT.

The contribution of the spectra corresponding to the different conformations of the porphyrin dimer at different wavelengths was predicted based on a combination of the results from TDDFT calculations reported in reference [11] and experimental results of UV-vis measurements.

The positions of the absorption bands for different dihedral angles were predicted by TDDFT calculations.[11] It is well known that TDDFT often does not predict absolute energies correctly [12] and hence for the purpose of this analysis the width of the predicted distribution and the absolute positions were scaled to match the experimental room temperature UV-vis spectrum as shown in Figure S6 A. The UV-vis spectrum could be reconstructed as a sum of Gaussians centred at the predicted positions, but this would not explain the presence of an EPR spectrum corresponding to the planar dimer conformation at wavelengths from about 600 to 700 nm. As discussed above, the low temperature UV-vis spectrum was attributed to the vibronic absorption band of the pure planar conformation. Therefore instead of a Gaussian, the corresponding absorption band with its vibrational structure, taken from the low temperature UV-vis spectrum shown in Figure 1, was used to model the contributions of different conformations at different wavelengths.[13] The intensities for the absorption bands corresponding to the different conformations were determined based on the oscillator strengths predicted by DFT and on a weighting factor calculated from a Boltzmann population distribution at different temperatures (with a 0.67 kcal/mol ground state barrier for rotation around the central butadiyne bond)[11]. The model UV-vis spectrum thus constructed was used to predict the EPR and ENDOR spectra for excitation at different wavelengths. The calculated EPR spectra for each conformation were summed based on the relative weights determined from the reconstructed UV-vis spectrum at different wavelengths and the results are shown in Figure S6 B and C.

The changes observed in the time-resolved EPR spectra of the

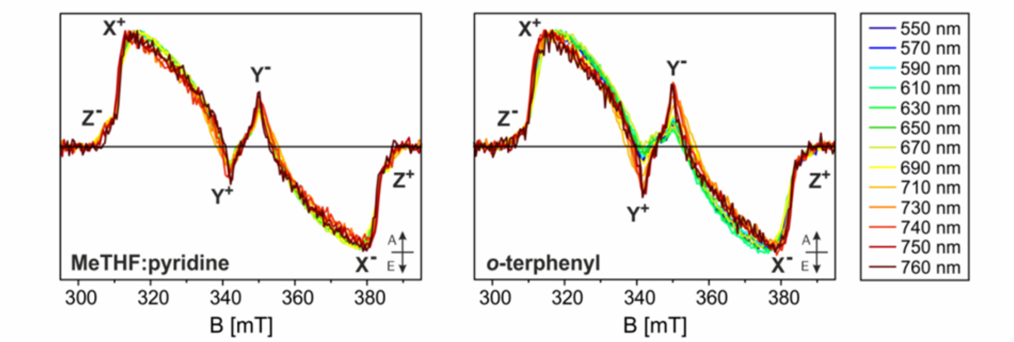

**Figure S5.** Transient EPR spectra recorded at 20 K for **P2** in MeTHF:pyridine 10:1 (left) and in *o*-terphenyl (right) using different excitation wavelengths. The spectra were recorded using light polarized parallel or perpendicular to the magnetic field and averaged up to 2 µs after the laser pulse and the depolarized spectra shown here were reconstructed as $\frac{1}{3}(I_{\parallel}+2I_{\perp})$ . The spectra were normalized to the maximum. (A=absorption, E=emission)

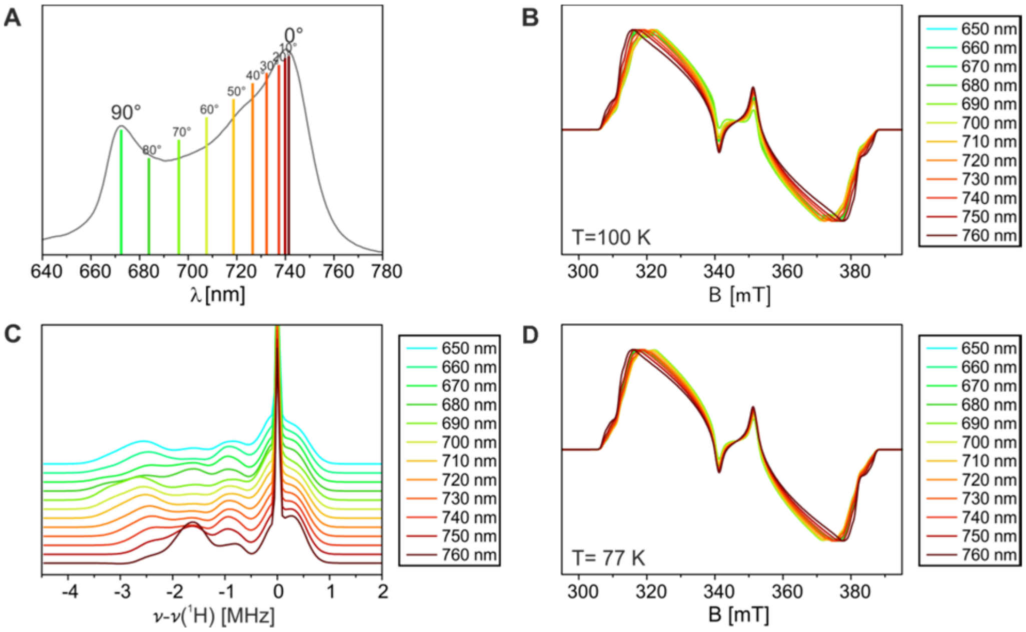

**Figure S6.** (A) Q-band of the **P2** absorption spectrum recorded at room temperature (grey) and stick spectrum indicating the positions of the absorption bands for different conformations of the porphyrin dimer. The relative positions of these absorption bands have been derived from the TDDFT calculations reported in reference [11] and the width and absolute positions have been scaled to match the experimental room-temperature UV-vis spectrum for further analysis. The relative intensities reflect the oscillator strengths predicted by DFT. (B) Calculated EPR spectra of **P2** for excitation at different wavelengths using the model described in the text for Boltzmann distributions at 100 K (B) and 77 K (D). (C) Calculated ENDOR spectra of **P2** for excitation at different wavelengths using the model described in the text (Boltzmann distribution at 100 K).

two different solvent systems, MeTHF:pyridine with a glass transition temperature of about 100 K and *o*-terphenyl with a glass transition temperature of 246 K [14] (see Figure 2A and Figure S5) can be qualitatively reproduced by calculations for two different Boltzmann distributions, at 100 and at 77 K (see Figure S6). The disagreement between the glass transition temperatures of the solvent systems and the temperatures needed to reproduce the observed changes are due to the numerous approximations necessary to model the relative contribution of different conformations at different wavelengths. At the wavelengths with the largest contribution of the twisted conformation, the intensity of the central Y transitions decreases and the X transitions are shifted towards the centre. The analysis described above indicates that the observed changes are caused by the contribution of a distribution of EPR spectra that tend towards the EPR spectrum observed for the porphyrin monomer.

The calculated ENDOR spectra in Figure S6 C also predict a broadening and the appearance of an additional peak at larger hyperfine couplings, as observed experimentally (Figure 4 B). The poor quantitative agreement of calculation and experiment can be attributed to the large number of approximations required to perform this analysis. Nevertheless the experimentally observed wavelength dependence could be qualitatively explained and the contribution of a distribution of different orientations to both EPR and ENDOR spectra could be confirmed.

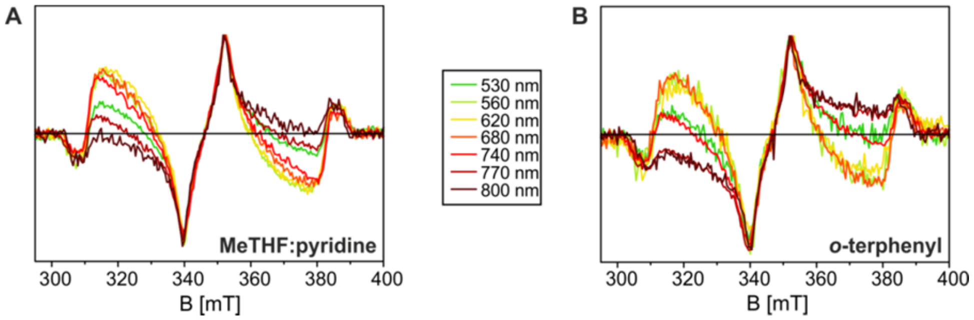

**Figure S7.** Transient EPR spectra recorded at 20 K for **P3** in MeTHF:pyridine 10:1 (A) and in *o*-terphenyl (B) using different excitation wavelengths. The spectra were recorded using light polarized parallel or perpendicular to the magnetic field and averaged up to 2 µs after the laser pulse and the depolarized spectra shown here were reconstructed as $\frac{1}{3}(I_{\parallel}+2I_{\perp})$ . The spectra normalized to the maximum.

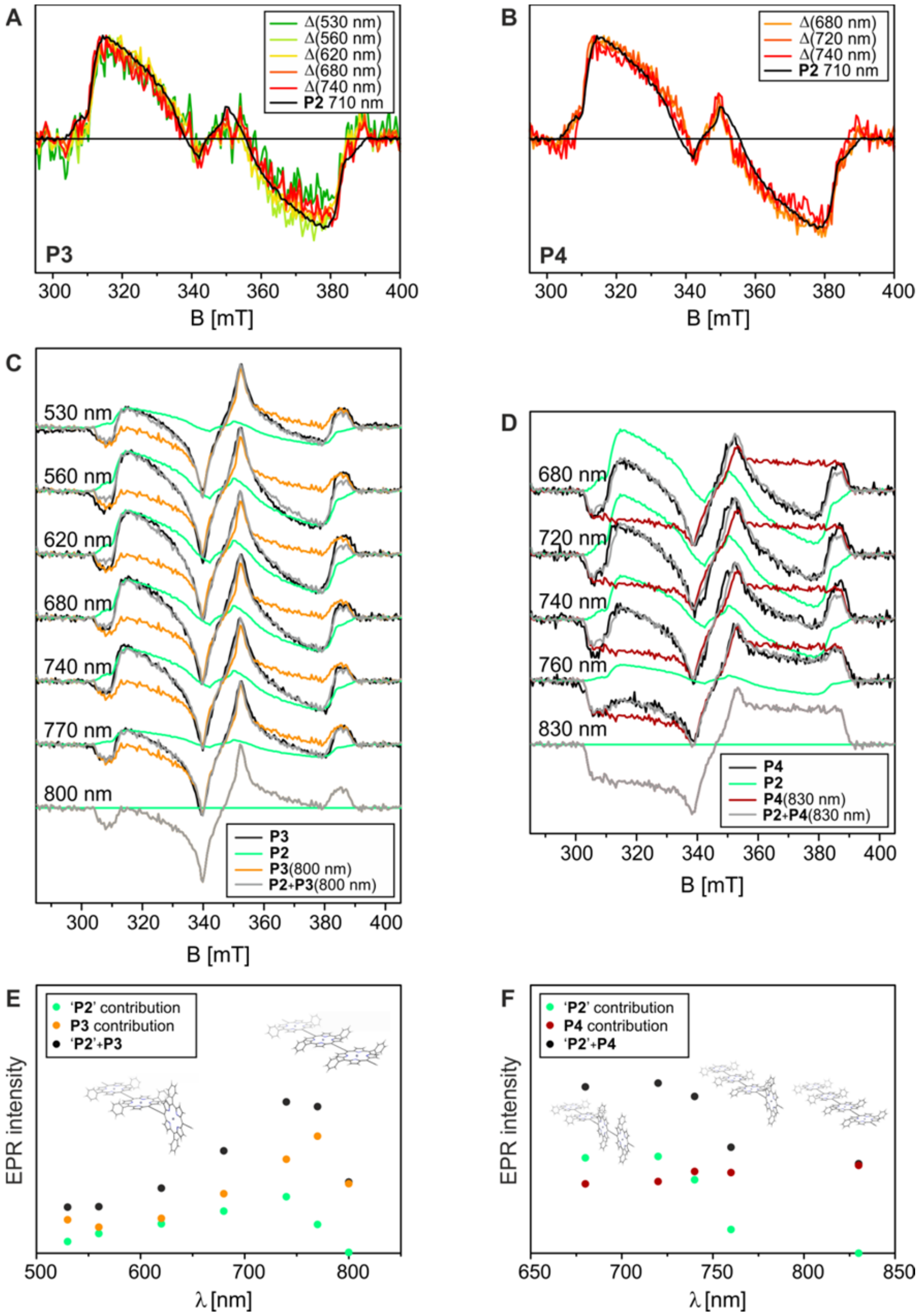

**Figure S8.** (A/B) EPR spectra obtained by subtraction of the normalized **P3**/**P4** spectrum recorded at 800/830 nm from the EPR spectra recorded for excitation at lower wavelengths. The resulting subtraction spectra are compared to the **P2** spectrum recorded after excitation at 710 nm. (C/D) Reconstruction of the time-resolved EPR spectra recorded for **P3**/**P4** at different wavelengths as a linear combination of the **P3**/**P4** spectrum recorded at 800/830 nm and the **P2** spectrum. (E/F) Contributions of the '**P2**' (= dimer-like) and planar **P3**/**P4** conformations, resulting from the linear combinations shown in C and D, to the EPR signal intensity (divided by the laser power) as a function of wavelength. Representative structures of **P3** and **P4** contributing at different wavelengths are also shown.

## References

1. F. C. Grozema, C. Houarner-Rassin, P. Prins, L. D. A. Siebbeles and H. L. Anderson, *J. Am. Chem. Soc.*, 2007, **129**, 13370-13371.
2. C. E. Tait, P. Neuhaus, M. D. Peeks, H. L. Anderson and C. R. Timmel, *J. Am. Chem. Soc.*, 2015, **137**, 8284-8293.
3. F. Neese, 2.9/3.0 edn., 2011.
4. F. Neese, *Wiley Interdiscp. Rev.: Comput. Mol. Sci.*, 2012, **2**, 73-78.
5. S. Sinnecker and F. Neese, *J. Phys. Chem. A*, 2006, **110**, 12267-12275.
6. V. Barone, in *Recent Advances in Density Functional Methods, Part I*, ed. D. P. Chong, World Scientific Publ. Co., Singapore, 1996.
7. V. Barone, *J. Chem. Phys.*, 1994, **101**, 6834-6838.
8. V. Barone, *J. Chem. Phys.*, 1994, **101**, 10666-10676.
9. S. Stoll and A. Schweiger, *J. Magn. Reson.*, 2006, **178**, 42-55.
10. C. E. Tait, P. Neuhaus, H. L. Anderson and C. R. Timmel, *J. Am. Chem. Soc.*, 2015, **137**, 6670-6679.
11. M. U. Winters, J. Kärnbratt, M. Eng, C. J. Wilson, H. L. Anderson and B. Albinsson, *J. Phys. Chem. C*, 2007, **111**, 7192-7199.
12. S. Grimme and M. Parac, *Chem. Phys. Chem.*, 2003, **4**, 292-295.
13. M. D. Peeks, P. Neuhaus and H. L. Anderson, *Phys. Chem. Chem. Phys.*, 2016, **18**, DOI: 10.1039/C1035CP06167x.
14. H. Xi, Y. Sun and L. Yu, *J. Chem. Phys.*, 2009, **130**, 094508.